Climate Dynamics (2001) 17: 515–526

G. A. Meehl · P. R. Gent · J. M. Arblaster
B. L. Otto-Bliesner · E. C. Brady · A. Craig

# Factors that affect the amplitude of El Nino in global coupled climate models

Received: 17 April 2000 / Accepted: 17 August 2000

**Abstract** Historically, El Nino-like events simulated in global coupled climate models have had reduced amplitude compared to observations. Here, El Nino-like phenomena are compared in ten sensitivity experiments using two recent global coupled models. These models have various combinations of horizontal and vertical ocean resolution, ocean physics, and atmospheric model resolution. It is demonstrated that the lower the value of the ocean background vertical diffusivity, the greater the amplitude of El Nino variability which is related primarily to a sharper equatorial thermocline. Among models with low background vertical diffusivity, stronger equatorial zonal wind stress is associated with relatively higher amplitude El Nino variability along with more realistic east–west sea surface temperature (SST) gradient along the equator. The SST seasonal cycle in the eastern tropical Pacific has too much of a semiannual component with a double intertropical convergence zone (ITCZ) in all experiments, and thus does not affect, nor is it affected by, the amplitude of El Nino variability. Systematic errors affecting the spatial variability of El Nino in the experiments are characterized by the eastern equatorial Pacific cold tongue regime extending too far westward into the warm pool. The time scales of interannual variability (as represented by time series of Nino3 SSTs) show significant power in the 3–4 year ENSO band and 2–2.5 year tropospheric biennial oscillation (TBO) band in the model experiments. The TBO periods in the models agree well with the observations, while the ENSO periods are near the short end of the range of 3–6 years observed during the period 1950–94. The close association between interannual variability of equatorial eastern Pacific SSTs and large-scale SST patterns is represented by significant correlations between Nino3 time series and the PC time series of the first EOFs of near-global SSTs in the models and observations.

## 1 Introduction

Early global coupled climate models simulated interannual variability in the tropical Pacific that was typically around 50% the amplitude seen in observations (e.g., Sperber et al. 1987; Meehl 1990; Lau et al. 1992; Nagai et al. 1992; Tett 1995). This systematic error has been noted to occur in global coupled models both with and without flux adjustment (Pontaud et al. 1998). It has been recognized that the class of relatively coarse grid global coupled models is not capable of simulating all the relevant dynamical coupled processes that contribute to observed El Nino events (Neelin et al. 1992). More recent global coupled model versions with enhanced latitudinal resolution in the equatorial tropics and other improvements have shown somewhat higher amplitude SST variability in the eastern equatorial Pacific and better success in simulating El Nino-like phenomena (Yukimoto et al. 1996; Roeckner et al. 1996; Timmermann et al. 1999; Latif et al. submitted 2000). However, simply looking at the amplitude of an index of El Nino activity, such as Nino3 SSTs (SST anomalies averaged over the area 5°S–5°N, 150°W–90°W), does not provide information on why some models simulate higher amplitude El Nino-like events than others.

Stability analysis has shown that the magnitude of El Nino events as measured by, for example, the Nino3 index, strongly depends on the basic state of the atmosphere and ocean (e.g., Neelin 1991; Wang and Feng 1996; Li 1997). In particular, coupled model experiments by Zebiak and Cane (1987) and Latif et al. (1993) showed that the amplitude of the El Nino cycle was very sensitive to the zonal mean thermocline depth in the equatorial Pacific. The intensity of the thermocline is of course related in part to the vertical mixing (e.g., Wilson 2000). Thus, this is a possible candidate for differences

---

G. A. Meehl (✉) · P. R. Gent · J. M. Arblaster
B. L. Otto-Bliesner · E. C. Brady · A. Craig
National Center for Atmospheric Research,
Boulder, CO 80307-3000, USA
E-mail: meehl@ncar.ucar.edu

between the El Nino amplitudes simulated by global coupled models. Another is the seasonal cycle in the eastern Pacific. Coupled models without flux adjustment have had difficulties simulating the seasonal cycle in the eastern tropical Pacific, and there is some speculation that improvements there could improve El Nino simulations (Mechoso et al. 1995). However, that study and subsequent ones (e.g., Pontaud et al. 1998; Latif et al. 2000) could not find a preferential relationship across the models between a good simulation of the seasonal cycle and a superior simulation of El Nino.

The problem in most of the intercomparison studies is that all the models and components are different, and it is difficult to isolate possible contributions from various factors. Here, we compare the El Nino simulations in a number of different versions of two global coupled models, the climate system model (CSM) and parallel climate model (PCM). Their main difference that affects the simulation of El Nino phenomena is in the ocean components. We will examine differences in the simulated seasonal cycles in the eastern Pacific, as well as possible contributions from the structure of the simulated thermocline in the equatorial Pacific to identify factors that contribute to differences of El Nino amplitude.

## 2 Models and experiments

The CSM and PCM are fully coupled global ocean-atmosphere-sea ice-land surface models and use the CCM3 for the atmospheric component. The PCM and standard CSM use T42 resolution (an equivalent grid spacing of roughly 2.5 by 2.5°) and 18 levels (hybrid coordinates; see details and references in Kiehl et al. 1998). The PaleoCSM uses the T31 resolution CCM3 with 18 vertical levels (Otto-Bliesner 1999). The CSM and PCM use the same land surface component, the LSM, with specified vegetation types and a comprehensive treatment of surface processes (see Bonan 1998).

The ocean component in all CSM experiments is the NCAR CSM ocean model (NCOM, Gent et al. 1998). The standard CSM experiment uses the NCOM × 2 grid, which has 45 vertical levels, a 2.4° longitudinal grid spacing and a maximum latitudinal grid spacing of 2.4° at mid-latitudes that decreases to 1.2° near the equator. The newer CSM version uses the NCOM × 2′ grid which is like the NCOM × 2 grid, except for a finer latitudinal spacing of 1.2° poleward of 30° smoothly decreasing to 0.6° within 10° of the equator. The PaleoCSM uses the NCOM × 3′ grid which has 25 vertical levels, 3.6° longitudinal grid spacing and a latitudinal spacing of 1.8° poleward of 30° decreasing to 0.9° within 10° of the equator. All these CSM versions employ the Gent-McWilliams (GM) eddy parametrization and a KPP boundary layer scheme (see details and references in Gent et al. 1998). Both the NCOM × 2′ and NCOM × 3′ versions use a spatially varying horizontal viscosity scheme (Large et al. 2000) which makes the equatorial currents much more realistic compared to the NCOM × 2 version.

The most notable difference between the PCM and CSM in the context of El Nino is in the ocean component. The PCM ocean component (Washington et al. 2000) is a version of the parallel ocean processor (POP) with 32 levels in the vertical and 2/3° nominal latitude-longitude resolution reducing to 0.5° in latitude in the tropics (actual longitudinal grid spacing in the equatorial Pacific ranges from about 0.6° in the east to 0.9° in the west due to the effects of the rotated pole over northern North America). The PCM ocean component uses biharmonic diffusion horizontal mixing and Pacanowski-Philander vertical mixing (see Semtner 2000). Upper ocean vertical resolutions for the CSM versions and the PCM are shown in Fig. 1. The CSM/NCOM × 2 and ×2′ have 19 levels in the upper 500 m and seven levels in the upper 100 m, the CSM/NCOM × 3′ has 10 and 5, respectively, while the PCM has 13 and 4. PCM experiment 10 in Table 1 has four extra levels added in the upper 100 m so that there are then eight levels in the upper 100 m.

The sea-ice component in CSM includes Semtner three-layer thermodynamics and the Flato–Hibler cavitating fluid ice rheology (see Weatherly et al. 1998). The PCM has a somewhat different sea-ice scheme but also with thermodynamic and dynamic parts (see Weatherly and Washington submitted 2000). It is thought that the sea-ice formulation does not contribute to the differences in El Nino phenomena in the models.

The spin-up procedure for the CSM versions starts with an ocean equilibrium state, whereas the PCM versions use an initial state taken from a short run with restoring back to observed temperature and salinity at all grid points. Then all models are spun up with an accelerated deep ocean with repeated forcing from five years of an atmospheric model integration (for more details see Boville and Gent 1998; Washington et al. 2000). No flux adjustments are used in the models. The CSM versions are run from the accelerated spin-up for the fully coupled experiments analyzed here. After the first 50 years of the PCM fully coupled integration, an adjustment to background aerosol was made, and then the experiments analyzed here were started from that point.

A list of the ten model experiments are given in Table 1. Experiments 1, 2, 6, and 8 are long control integrations of 200 years or more, whereas the others are sensitivity experiments of relatively short duration. However, the sensitivity experiments reveal systematic behaviors that allow us to draw conclusions about factors that affect the amplitude of El Nino. The improvements indicated in these sensitivity experiments are being applied in subsequent multi-century coupled model simulations.

As noted in Table 1, the ocean model background vertical diffusivity parameter is varied among the model experiments,

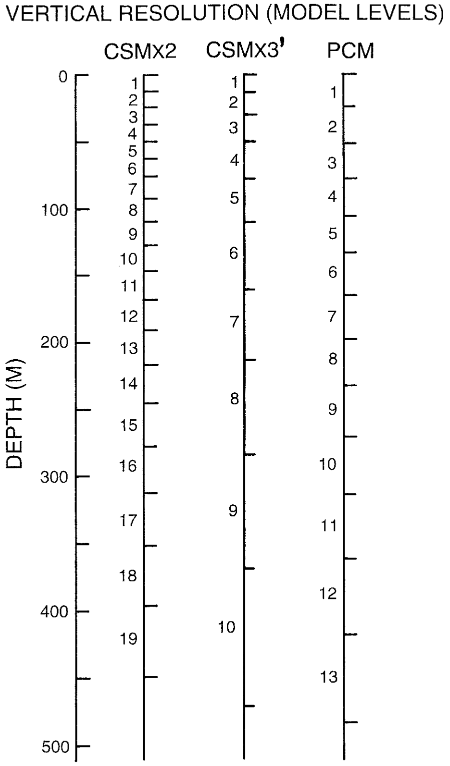

**Fig. 1** Upper ocean vertical resolution for the model versions used in the experiments listed in Table 1. Note that CSM × 2 and CSM × 2′ have the same vertical resolution

**Table 1** Model experiments

| Experiment number | Model | Atmosphere CCM3 | Ocean | Background vertical diffusivity $cm^2\ s^{-1}$ | Years analyzed |
|---|---|---|---|---|---|
| 1 | CSM | T42 18L | NCOM × 2 (2.4°, 1.2°, 45L) | 0.3 | 45 |
| 2 | Paleo CSM | T31 18L | NCOM × 3′ (3.6°, 0.9°, 25L) | 0.5 | 40 |
| 3 | Paleo CSM | T31 18L | NCOM × 3′ (3.6°, 0.9°, 25L) | 0.3 | 40 |
| 4 | Paleo CSM | T31 18L | NCOM × 3′ (3.6°, 0.9°, 25L) | 0.2 | 40 |
| 5 | Paleo CSM | T31 18L | NCOM × 3′ (3.6°, 0.9°, 25L) | 0.15 | 40 |
| 6 | Paleo CSM | T31 18L | NCOM × 3′ (3.6°, 0.9°, 25L) | 0.1 | 40 |
| 7 | CSM | T42 18L | NCOM × 2′ (2.4°, 0.6°, 45L) | 0.1 | 30 |
| 8 | PCM | T42 18L | POP (2/3°, 1/2°, 32L) | 0.1 | 45 |
| 9 | PCM | T42 18L | POP (2/3°, 1/2°, 32L) | 0.3 | 23 |
| 10 | PCM | T42 18L | POP (2/3°, 1/2°, 36L, 4 extra in upper 100 m) | 0.1 | 23 |

ranging from values of 0.1 to 0.5 $cm^2\ s^{-1}$. A number of different aspects of the model simulations that could play a role in the manifestation of El Nino will be examined later, the primary one being the magnitude of background vertical diffusivity. Other aspects of El Nino such as the zonal wind stress, the seasonal cycle in the eastern Pacific, and spatial patterns and time scales also will be examined.

## 3 Factors affecting the amplitude of El Nino variability

### 3.1 Ocean background vertical diffusivity

In comparing the various global coupled model experiments depicted in Table 1, the dominant influence on El Nino amplitude is the magnitude of the ocean model background vertical diffusivity, as shown in Fig. 2. Across all model experiments, regardless of resolution or ocean physics, the runs with the lowest values of background vertical diffusivity have the largest Nino3 amplitudes.

To obtain the Nino3 and Nino4 time series for all model experiments, the monthly mean uppermost ocean level potential temperatures (SST) are averaged over the appropriate area, the mean monthly cycle is removed and a five month boxcar smoother is applied, as in Trenberth (1997). To give a range of possible observed values, we compute Nino3 (5°S–5°N, 150°W–90°W) for two periods (observed SST indices are obtained from NOAA and smoothed in a similar manner; Reynolds and Smith 1994). The observed Nino3 standard deviation for the period 1950–98 is 0.86 °C, and for 1950–79 it is 0.70 °C. This observed range is near the values for model experiments with a background vertical diffusivity of 0.1 $cm^2\ s^{-1}$ that range from 0.94 to 0.69 °C. Nino3 standard deviations for all other model versions with background vertical diffusivity values greater than 0.1 $cm^2\ s^{-1}$ fall below the model experiments that use 0.1 $cm^2\ s^{-1}$. The lowest simulated Nino3 standard deviation is 0.43 °C from experiment 2, and that model version has the highest background vertical diffusivity value of 0.5 $cm^2\ s^{-1}$.

Results for Nino4 (SST anomalies averaged over the area 5°S–5°N, 150°W–160°E, shown in Fig. 2b) are similar, with the observed range of 0.55 to 0.59 °C which is near the values for the models using background vertical diffusivity of 0.1 $cm^2\ s^{-1}$ that range from 0.47 to 0.66 °C. The results for Nino4 are not as monotonic as those for Nino3, because experiment 1, with higher values of background vertical diffusivity, has an amplitude comparable with the observations. However, a low Nino4 standard deviation of 0.38 °C occurs in experiment 2, which has the highest diffusivity value of 0.5 $cm^2\ s^{-1}$.

Comparing specific versions of the same model with different values of background vertical diffusivity also illustrates this result. The most directly comparable model versions are the variants of the PaleoCSM (experiments 2 through 6), where the only difference between the experiments is the background vertical diffusivity value. Figure 2a, b shows a monotonic decrease of Nino3 and Nino4 amplitudes as the background vertical diffusivity is increased from 0.1 to 0.5 $cm^2\ s^{-1}$. In addition, for these experiments the ratio of variability in the eastern tropical Pacific (Nino3) compared to the central tropical Pacific (Nino4) increases as the background vertical diffusivity is decreased from 0.5 to 0.1 $cm^2\ s^{-1}$, closer to the ratio for observations.

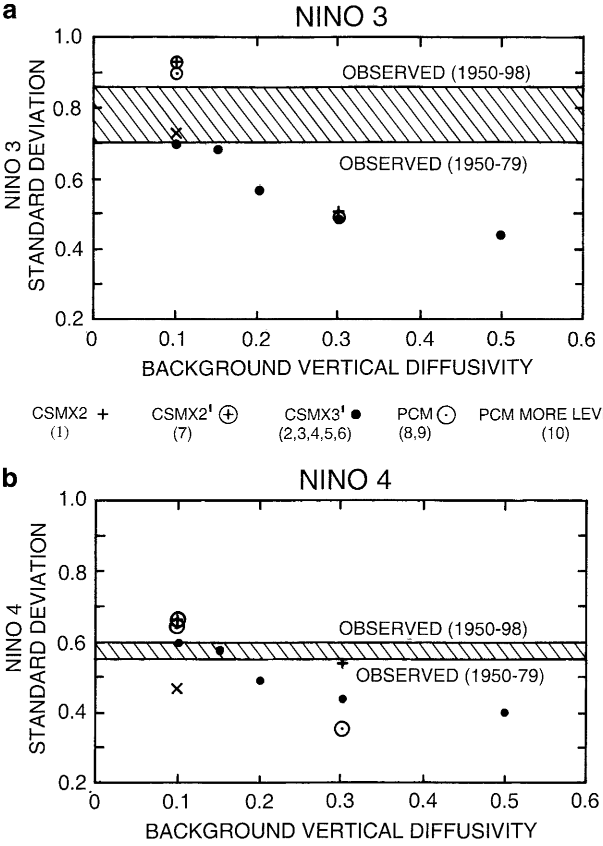

**Fig. 2** **a** Ocean model background vertical diffusivity versus Nino3 amplitude for all experiments. The *solid lines* represent Nino3 amplitude for the observations from 1950–1998 and 1950–1979. **b** Same as **a** but for Nino4

Similar results are seen for experiments 8 and 9. The experiment with the lower value of background vertical diffusivity of 0.1 $cm^2\ s^{-1}$ (experiment 8) has higher Nino3 and Nino4 amplitudes (0.90 °C and 0.65 °C, respectively) than the experiment with higher background vertical diffusivity of 0.3 $cm^2\ s^{-1}$ (experiment 9), which has lower Nino3 and Nino4 amplitudes of 0.50 °C and 0.35 °C, respectively.

How does the value of background vertical diffusivity affect Nino3 and Nino4 amplitudes? To address this question, the upper ocean temperature structure along the equator is shown in Fig. 3a for observations, Fig. 3b for experiment 8, and Fig. 3c for experiment 6. These two experiments are chosen as representative of the PCM and PaleoCSM simulations, respectively. Both experiments 6 and 8 produce a fairly good representation of the equatorial Pacific thermocline intensity and its upward tilt to the east, although the experiment 8 upper ocean temperatures are somewhat colder than those in experiment 6, and observations.

To measure the intensity of the thermocline for the models, we compute the depth range, or thicknesses, of the 16 to 22 °C temperature interval at 155°W in the central equatorial Pacific. The Nino3 amplitude is represented here and throughout the study as the standard deviation of the smoothed Nino3 monthly SSTs as defined earlier. For observations this value is 70 m, the same value for experiments 6 and 8. Thus, both models have thermoclines that are of comparable intensity to observations, but experiment 8 has greater Nino3 amplitude (0.90 °C) compared to experiment 6 (0.69 °C), even though they both have the same background vertical diffusivity of 0.1 cm$^2$ s$^{-1}$. The depth of the thermocline can be diagnosed as the depth of the 20 °C isotherm at 155°W. In the observations it is 120 m, in experiment 6 it is near 110 m, but in experiment 8 it is about 50 m, and this is reflected by the colder SSTs at the surface in experiment 8 (Fig. 3). Thus, the depth of the thermocline, as well as its intensity, is an important factor in determining Nino3 amplitude.

These changes in equatorial SST variability are the result of strong changes in the mean structure of the equatorial thermocline in the Pacific in the ten experiments. Figure 4 shows the indices of thermocline intensity and the mean depth of the thermocline (depth of the 20 °C isotherm at 155°W), plotted here for all ten experiments as a function of Nino3 amplitude. The range for the observations of Nino3 amplitude also is shown for the two time periods

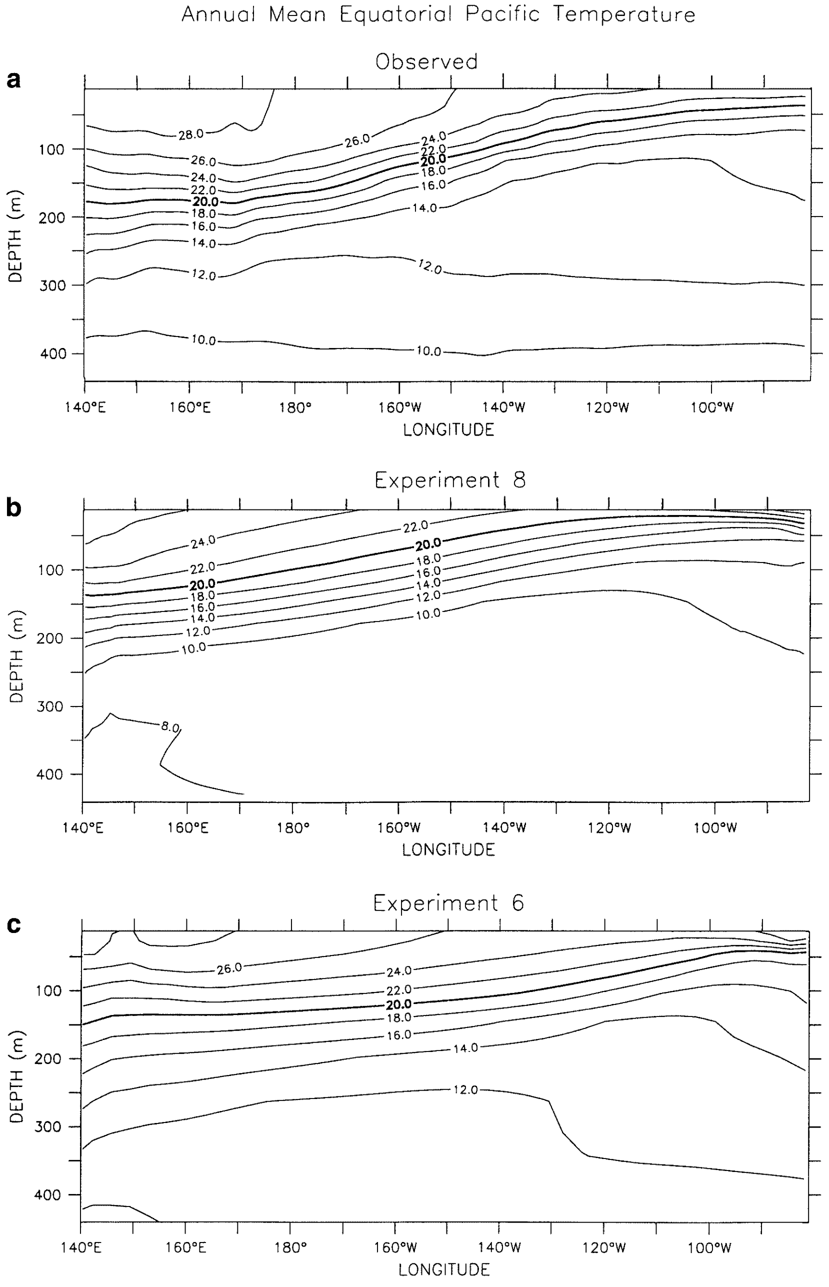

**Fig. 3a–c** Upper ocean equatorial Pacific temperature structure in °C for **a** observations (Levitus 1982) **b** experiment 8 and **c** experiment 6. Temperatures are averaged over 2°S–2°N. The 20 °C isotherm is highlighted in *bold*

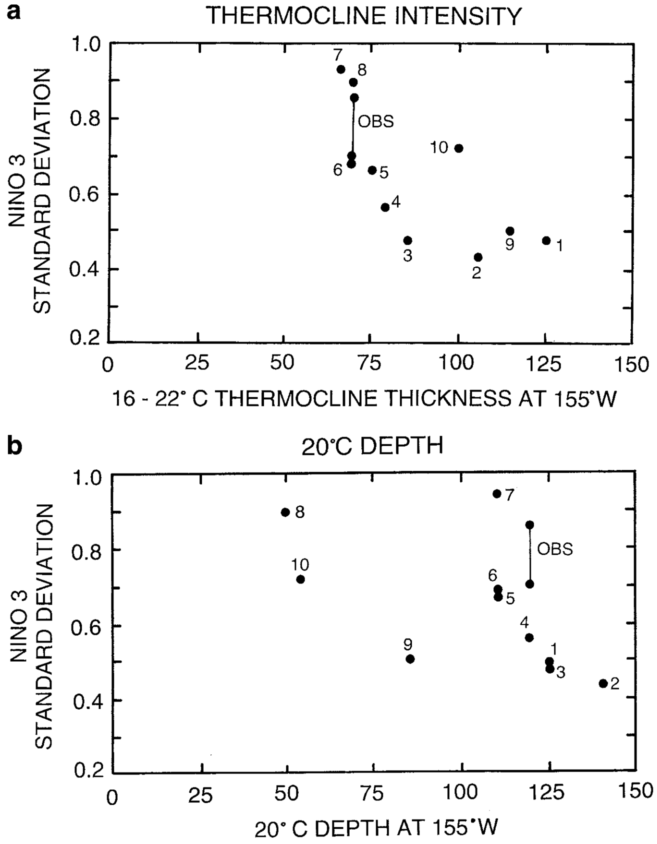

**Fig. 4** **a** Thermocline intensity (defined as the depth range between the 16 °C and 22 °C isotherms at 155°W) versus Nino3 amplitude (defined as standard deviation of Nino3 SSTs as defined in the text) for all experiments. **b** Mean depth of the 20 °C isotherm at 155°W versus Nino3 amplitude for all experiments. The observed range in **a** and **b** is shown for the two values of Nino3 amplitude defined for Fig. 2

defined for Fig. 2. Figure 4a shows that models with more intense thermoclines produce greater Nino3 amplitudes. The observations lie near the middle of the range of model realizations for thermocline depth as a function of Nino3 amplitude in Fig. 4b, but are closer to the model experiments with more intense thermoclines.

Experiment 8 does produce a thermocline intensity (Fig. 4a) that is close to the observed value. However, it has a systematic error of colder than observed temperature in the upper 400 m (Fig. 3b), which is reflected in the 20 °C isotherm being near the top of the thermocline in that model. If the depth of the strongest thermocline gradient is computed in experiments 8, 9 and 10 (the models that have this systematic error), their values in Fig. 4b shift about 50 m deeper. Then they align more closely with the values from the other models whose 20 °C isotherm is better captured in the main thermocline. Even with this adjustment, the relationship still holds that models with systematic upper ocean cold bias (e.g., experiments 8 and 10) can simulate near-observed Nino3 amplitude. This indicates that the Nino3 amplitude alone does not necessarily represent all ENSO-related characteristics of coupled climate models.

Figure 4 clearly shows that models with lower background vertical diffusivity and larger amplitude El Nino variability tend to have a shallower and/or more intense thermocline compared to the ones with higher background vertical diffusivity and lower amplitude El Nino variability. This implies that for a given wind variation, it is easier for equatorial upwelling to tap the colder sub-thermocline water in the models with the sharper and/or shallower thermoclines, thus contributing to higher amplitude SST variability.

### 3.2 Ocean vertical resolution and mixing schemes

In a model run directly comparable to experiment 8, four extra levels were added in the top 100 m of the ocean in experiment 10 to test the effects of vertical resolution. There is an effect on the upper ocean equatorial Pacific temperature structure in this experiment. The depth of the 20 °C isotherm at equator, 155°W deepens slightly to 55 m (from 50 m in experiment 8), and the 16–22 °C depth span diffuses to 100 m (from 70 m in experiment 8), as seen in Fig. 4. Thus the thermocline deepens somewhat and becomes less intense in this sensitivity experiment, and there are modest decreases of Nino3 and Nino4 amplitude in experiment 10 compared to experiment 8 (Fig. 2). Though higher vertical resolution in this model contributes to reduced El Nino amplitude, this effect is weaker than that occurring with an increase in background vertical diffusivity. The reductions are 44% for Nino3 and 46% for Nino4 amplitudes in the increased background vertical diffusivity experiment 9, and only a decrease of 20% for Nino3 and 28% for Nino4 amplitudes in the enhanced vertical resolution experiment, experiment 10.

Thus, there is strong evidence (also noted in earlier analyses of coarse grid coupled models, e.g., Meehl 1990) that if the vertical resolution is too coarse, upwelling reaches too deep and brings up water that is too cold, thereby contributing to increased SST variability solely due to the vertical resolution configuration (comparing cases 8 and 10). This was also noted to happen in the models where the thermocline is too shallow (Fig. 4b). Additionally, the KPP and Pacanowski and Philander mixing schemes have been shown to give quite similar mean thermocline structures (Large and Gent 1999), so that we do not expect these different vertical mixing schemes to be a large factor in governing the amplitude of El Nino variability.

### 3.3 Equatorial ocean horizontal resolution

In recent years, the equatorial meridional resolution in the ocean component of many coupled climate models has been increased, including the CSM. Is this necessary in order to obtain large amplitude El Nino variability? We cannot make a definitive conclusion from the ten experiments in Table 1, because in no pair of them is there just a change in ocean meridional resolution. However, the evidence from Fig. 4 is that the role of meridional resolution is weak in determining El Nino amplitude. For example, experiments 1, 3 and 9 have resolutions of 1.2°, 0.9° and 0.5°, yet all have comparable Nino3 amplitudes. These three experiments all have a background vertical diffusivity of 0.3 $\mathrm{cm}^2\ \mathrm{s}^{-1}$. For those experiments that use a diffusivity of 0.1 $\mathrm{cm}^2\ \mathrm{s}^{-1}$, Fig. 2a shows that experiment 6 with the most coarse meridional resolution does have the smallest Nino3 amplitude. However, this may be related to the weaker zonal wind stress in the T31 resolution atmosphere (see the next subsection). Figure 2b shows that the Nino4 amplitude is also not stratified according to the equatorial meridional resolution.

It would appear that, providing meridional resolution is not too coarse near the equator, it is not a large factor determining El Nino amplitude. Large et al. (2000) show that it might be more important for the meridional horizontal viscosity to remain small, rather than the resolution. They show that the NCOM × 2′ and NCOM × 3′ resolutions give comparable equatorial currents when using an anisotropic horizontal viscosity. Coarser meridional resolution does affect the numerical phase speed of the ocean equatorial waves, but this would affect the time scales of El Nino more than its amplitude. Higher meridional resolution will also allow a smaller horizontal viscosity because it is usually set to be the minimum value the resolution allows.

### 3.4 Zonal wind stress

Wind stress forcing also plays a role in the model experiments. Figure 5 shows zonal wind stress along the equator in the Pacific (averaged over 2°N–2°S) for the observations (Trenberth et al. 1989) and for three experiments; 6, 7, and 8. These three are chosen to be representative of the simulations in the other experiments,

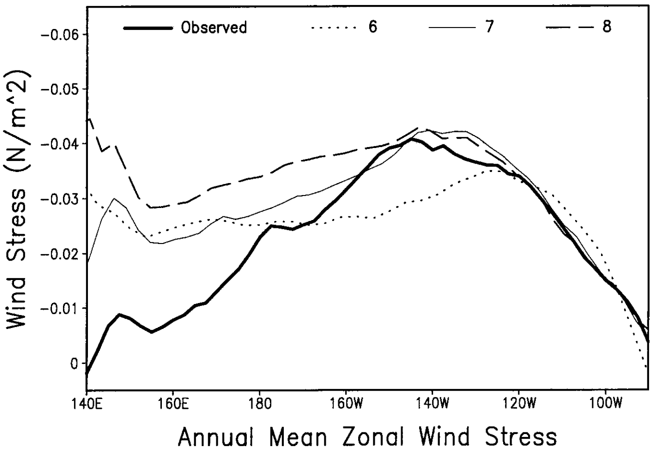

**Fig. 5** Mean zonal wind stress (N $m^{-2}$) in the equatorial Pacific (averaged over 2°S–2°N) for the observations (derived from the 1980–1989 ECMWF analyses, Trenberth et al. 1989; *thick solid line*), experiment 6 (*dotted*), experiment 7 (*thin solid line*) and experiment 8 (*dashed*)

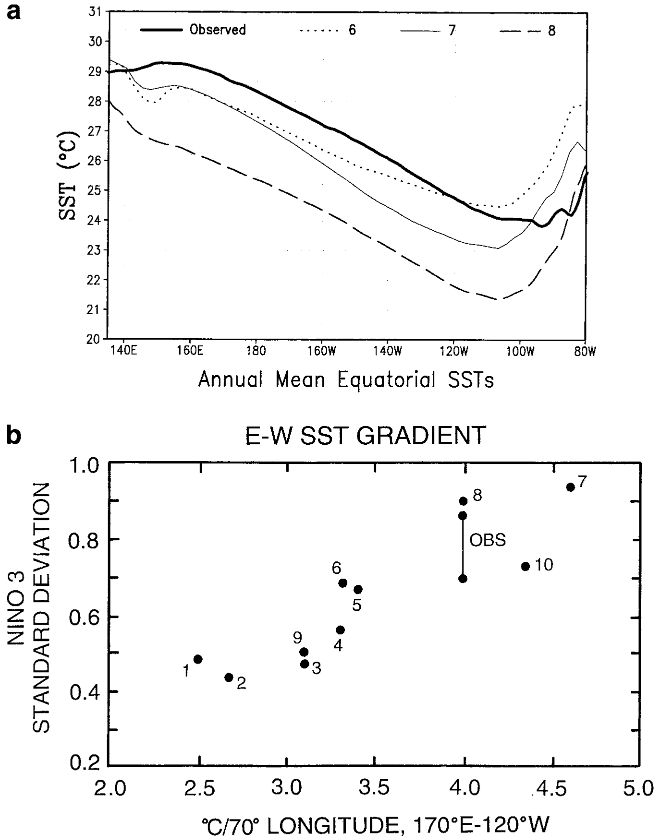

**Fig. 6** **a** Mean SSTs in the equatorial Pacific (averaged over 2°S–2°N) for the observations (1950–1979, Reynolds and Smith 1994; *thick solid line*), experiment 6 (*dotted*), experiment 7 (*thin solid line*) and experiment 8 (*dashed*). **b** The SST gradient between 170°E and 120°W versus Nino3 amplitude for all experiments

and these three all have 0.1 $cm^2$ $s^{-1}$ background vertical diffusivity and relatively large El Nino variability (Fig. 2). The three experiments show good agreement with the observed zonal wind stress values east of about 120°W with values ranging from near −0.015 N $m^{-2}$ at 100°W, to about −0.035 N $m^{-2}$ at 120°W. All experiments have stronger than observed zonal wind stress in the far western Pacific by factors ranging from about 2 to 3. However, between about the dateline and 125°W, experiments 7 and 8 have the strongest zonal wind stress (and stronger than observed) of around −0.028 to −0.035 N $m^{-2}$. In contrast experiment 6 has comparatively weaker zonal wind stress (and weaker than observed) with values ranging from about −0.03 to −0.023 N $m^{-2}$. Stronger than observed low level winds in the western equatorial Pacific are symptomatic of all the coupled models here, where the anomalous westward extent of the cold tongue regime is associated with a westward shift of the ascending branch of the Walker Circulation (Meehl and Arblaster 1998).

The mean strength of the zonal wind stress and its anomalies affect the coupling strength (e.g., Neelin et al. 1992) and should be expected to influence El Nino variability. The two experiments with the greater zonal wind stress from 120°W to the dateline (and stronger than observed), 7 and 8, have the largest Nino3 variability. Their Nino3 standard deviations are 0.94 °C and 0.90 °C, respectively, larger than the observed range in Fig. 2 of 0.70 to 0.86 °C. Meanwhile, experiment 6, with the weakest zonal wind stress of the three, has a lower amplitude Nino3 variability of 0.69 °C, which is just below the value of 0.70 °C at the low end of the observed range. Similar results are found for Nino4.

The equatorial SSTs across the Pacific (Fig. 6a) are shown for the same three representative experiments as in Fig. 5, and compared to observations from Reynolds and Smith (1994). The model experiments in Fig. 6a are all colder than observed between 170°E and 120°W, where the east–west SST gradient is strongest. East–west SST gradient is shown for all experiments as a function of Nino3 amplitude in Fig. 6b. It shows that the two experiments which best approximate the slope of the observed gradient from 170°E to 120°W (experiments 7 and 8 in Fig. 6a) have the largest Nino3 amplitudes. However, these two experiments are consistently colder than observations over this longitude range by about 1 °C and 3 °C, respectively. In the PaleoCSM experiment 6, the error in the slope of the east–west SST gradient is affected most by the SSTs in the western equatorial Pacific. The SST value of 24.7 °C at 120°W is close to the observed value there, but the SST at 170°E is about 1 °C too cold. In general, the thermocline slope in the models is proportional to the strength of the integrated zonal wind stress forcing across the equatorial Pacific. Experiment 8 with the strongest zonal wind stress (Fig. 5) has a thermocline slope of 105 m over the longitude range 120°W to 170°E. The value for experiment 7 with somewhat weaker zonal wind stress (Fig. 5) is 80 m, and for experiment 6, with even weaker zonal wind stress, the value is 60 m (compared to the observed value of about 110 m).

El Nino amplitude and associated east–west SST gradient along the equator is summarized for all ten model experiments in Fig. 6b where SST gradients are plotted in degrees celsius difference for 170°E minus 120°W spanning the longitudes where the zonal equatorial SST gradient is strongest (Fig. 6a). Figure 6b shows generally that models with stronger east–west equatorial SST gradients have larger El Nino amplitudes. However, different radiative forcings can affect east–west SST gradient without notable changes in El Nino amplitude (Meehl et al. 1993; Washington et al. 2000), and changes in thermocline slope unrelated to SST can also play a role (e.g., McPhaden 1999).

Though this is a coupled system and wind stress and SST are inextricably linked, we know from CCM3 atmosphere-alone experiments that there is a systematic error in the zonal wind stress which is too strong in the eastern equatorial Pacific (see Kiehl et al. 1998). This translates into a further westward extension of the cold tongue regime and wind stress errors in the coupled simulations in the central and western Pacific as noted in Fig. 5, consistent with the discussion in Meehl (1997a). Thus, the zonal wind stress forcing influences the relative Nino3 amplitude among models with the same background vertical diffusivity. The three experiments with 0.1 $cm^2$ $s^{-1}$ background vertical diffusivity (experiments 6, 7 and 8) produce Nino3 amplitudes consistent with their respective wind stress forcings (comparing Figs. 5 and 6b). The two experiments with stronger than observed wind stress from about the dateline to 120°W (7 and 8 in Fig. 5) have larger east–west SST gradients and greater amplitude of Nino3 variability (and greater than observed, Fig. 6). Meanwhile, the experiment with weaker than observed wind stress (6) has the weakest east–west SST gradient and the lowest amplitude Nino3 variability of the three representative experiments 6, 7 and 8.

However, as discussed already, the relationship between E–W SST gradient and Nino3 amplitude in Fig. 6b is not necessarily as straightforward as the relationship between Nino3 amplitude and thermocline intensity in Fig. 4. For example, Fig. 6 shows that the PaleoCSM experiments with lower Nino3 amplitude (2 and 3) have a range of the E–W SST gradient measure from 2.7 to 3.2 °C, while experiments 4 through 6 with higher Nino3 amplitudes have a more consistent E–W SST gradient measure of 3.3 °C. This suggests there may be some threshold of E–W SST gradient necessary for adequate simulations of Nino3 amplitude.

## 4 Spatial structure of El Nino variability

It was noted earlier that there may be a link between the simulation of the mean seasonal cycle in the eastern equatorial Pacific and some models' ability to simulate El Nino phenomena. Figure 7a shows monthly anomalies (the annual mean is subtracted) from the SST climatology of Reynolds and Smith (1994). In the first half of the year, relatively warmer SSTs move progressively westward to be replaced by cooler SSTs that move westward in the second half of the year. Figure 7b, c shows comparable plots from experiments 6 and 8. These are chosen to represent general features in all the model simulations, regardless of configuration. There is more of a semiannual signal in the model experiments, with the warmer SSTs in the first half of the year moving westward about two months later than in the observations. However, the re-establishment of the cooler water occurs at about the right time in the second half of the year, but shows even stronger westward propagation than the observations. This type of seasonal cycle, with the warm water progression delayed about two months at the beginning of the year and more of a semiannual signature, is characteristic of several of the global coupled models in Mechoso et al. (1995) and Latif et al. (2000). It is also a persistent systematic error in all the model versions considered here. In any case, the changes in El Nino amplitude in the experiments in Fig. 2 and model resolution changes appear to have little to do with the simulation of the seasonal cycle of SST in the eastern equatorial Pacific.

The seasonal cycle of precipitation in a sector of the eastern Pacific averaged from 150°W to 100°W is shown in Fig. 8a for the observations of Xie and Arkin (1996) and in Fig. 8b, c for the two model experiments 6 and 8. Long term monthly means are shown. The general characteristics of a stronger ITCZ north of the equator during the second half of the year, and a double ITCZ during northern spring are reproduced by both models. However, both also tend to produce a southern ITCZ year round. It is particularly strong in northern spring, with the ITCZ maxima somewhat farther poleward than the observed; near 10–12°S in northern spring, and

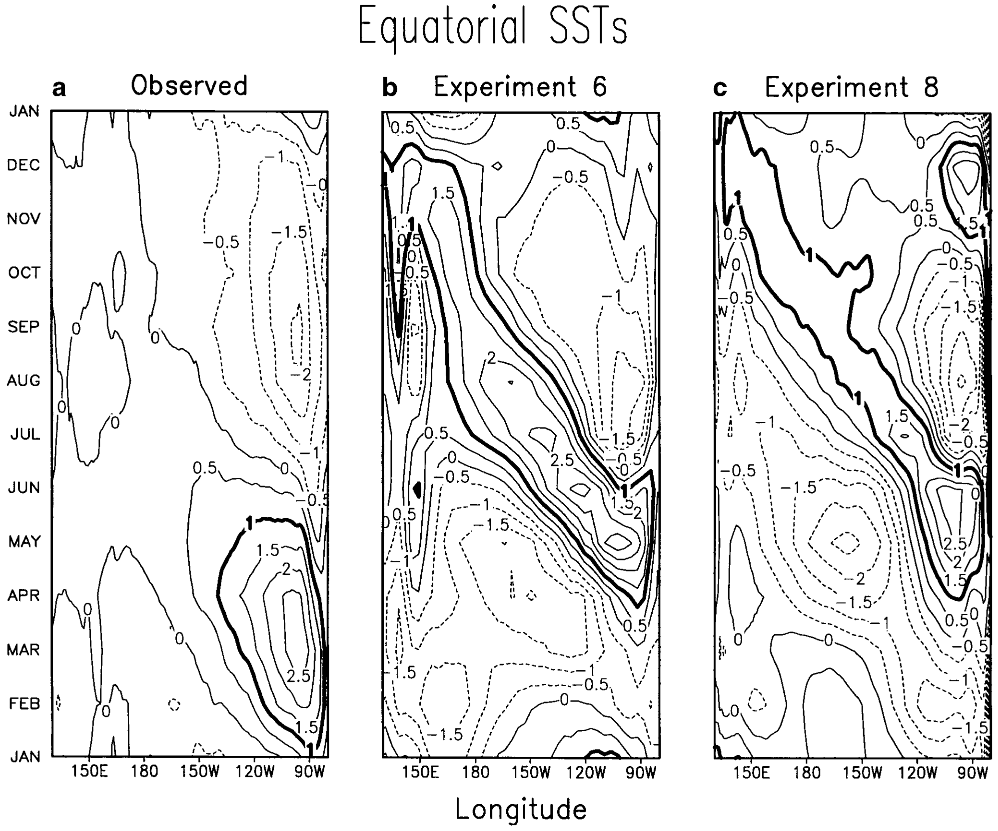

**Fig. 7a–c** Monthly anomalies of equatorial Pacific SSTs (°C) averaged over 2°S–2°N for the observations (1950–1979, Reynolds and Smith 1994; *left*), experiment 6 (*middle*) and experiment 8 (*right*). The 1 °C anomaly is highlighted in *bold*. Time runs *up the page*

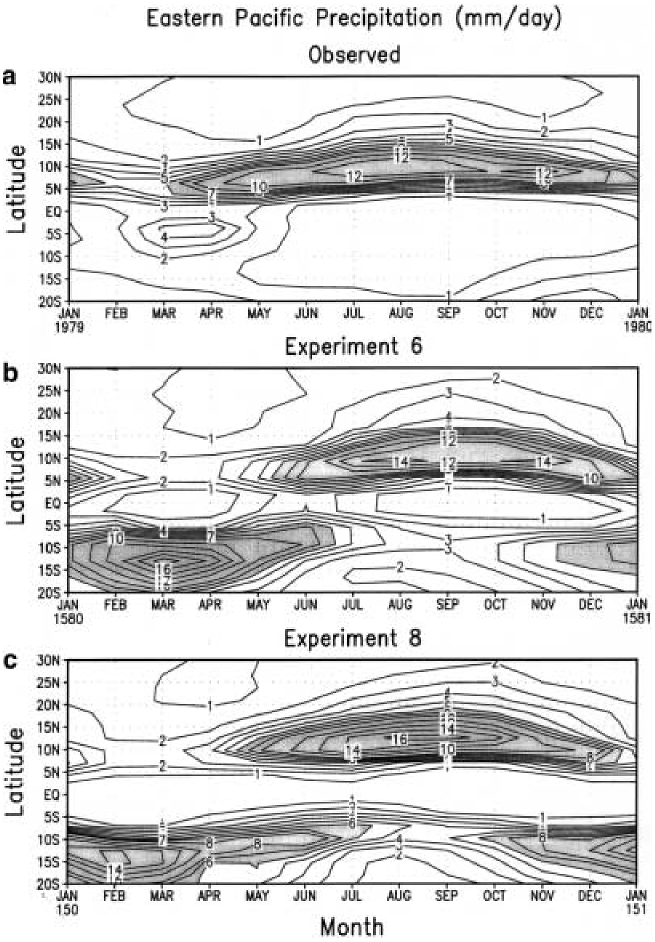

**Fig. 8a–c** Mean seasonal cycle of precipitation averaged over the Pacific sector from 150°W–100°W in mm/day for the observations (1979–1998; Xie and Arkin 1996; *top*), experiment 6 (*middle*) and experiment 8 (*bottom*). Values greater than 6 mm/day are *shaded*

around 10–12°N for the northern ITCZ, compared to about 5°S and 8–10°N, respectively, for the observations. Mechoso et al. (1995) show that the double ITCZ also is a typical problem in many global coupled models without flux adjustment. This could be partly related to the problems associated with inaccurate simulation of stratus clouds off the coast of South America, or with details of the convective parametrization and the SST errors that result south of the equator in the eastern Pacific (Ma et al. 1996; Yu and Mechoso 1999). The amplitude of the seasonal cycle is only marginally greater than the observed in the ITCZ maxima north of the equator with annual maximum values of about 12 mm day$^{-1}$ for the observations and roughly 14 mm day$^{-1}$ for the two model experiments. The seasonal cycle of precipitation in the eastern Pacific has similar systematic errors in all the experiments in this paper and does not contribute to the changes in El Nino amplitude.

Patterns of SST variability associated with the El Nino indices are illustrated by an EOF analysis in Fig. 9. To separate the interannual from the low frequency signals, we use an 8 year, 73 point low pass Lanczos filter applied to the monthly anomalies of SST from the observations and the three experiments (6, 7, and 8) with higher amplitude Nino3 variability, and all using background vertical diffusivity of 0.1 cm$^2$ s$^{-1}$. Once again, these three are chosen to represent comparable behavior in all the model versions. The high pass filtered time series are then formed by subtracting the low pass filtered data from the original time series. EOFs are calculated from the filtered data (over the latitudinal domain 40°S–60°N) using the correlation matrix technique. The corresponding principle component (PC) time series are then correlated with the filtered time series to form the patterns shown in Fig. 9.

EOF1 and the PC time series from the observed surface temperature dataset of Reynolds and Smith (1994) are shown in Fig. 9a, b for the 45 year period 1950–94 (36 months are removed from each end of the time series due to filtering). Concentrating on the tropical Pacific, the familiar El Nino-like pattern is evident with large positive values in the central and eastern equatorial Pacific, and opposite sign values in the north and south Pacific. The PC time series in Fig. 9b shows interannual variability readily identified with ENSO. A similar EOF analysis for a 45 year time series from experiment 8 in Fig. 9c also shows the El Nino-like pattern comparable to the observations in Fig. 9a. One crucial difference in the patterns in Fig. 9a, c is that the model has enhanced variability associated with the eastern equatorial Pacific cold tongue regime (defined as the westward extent of high equatorial SST variability) extending across the entire Pacific penetrating well into the western Pacific warm pool. This is a typical systematic error in global coupled models (e.g., Knutson and Manabe 1998), and results in a westward shift of the ascending branch of the Walker circulation in the western Pacific, and associated errors in the eastern equatorial Indian ocean compared to observations (Meehl and Arblaster 1998). Results for experiment 7 (30 year time series) in Fig. 9e are similar, with the cold tongue regime extending too far west, and comparable errors in the eastern Indian Ocean. The pattern of EOF1 is also similar in experiment 6 (45 year time series, Fig. 9g), but the cold tongue regime does not extend quite as far to the west as in experiments 7 or 8. This is consistent with the weaker zonal wind stress in experiment 6 compared to experiments 7 and 8 from about the dateline to 120°W shown in Fig. 5. Thus experiments 7 and 8 have stronger equatorial Pacific zonal wind stress and larger Nino3 variability, but also have a more pronounced systematic error of the cold tongue regime extending too far to the west. In contrast, experiment 6 has weaker equatorial Pacific zonal wind stress, relatively lower amplitude Nino3 variability, but less of the systematic error of the over-extensive eastern Pacific cold tongue regime seen in experiments 7 and 8.

To quantify the time scales of ENSO variability, spectra are calculated from the observed monthly Nino3 SST anomalies and from the three representative

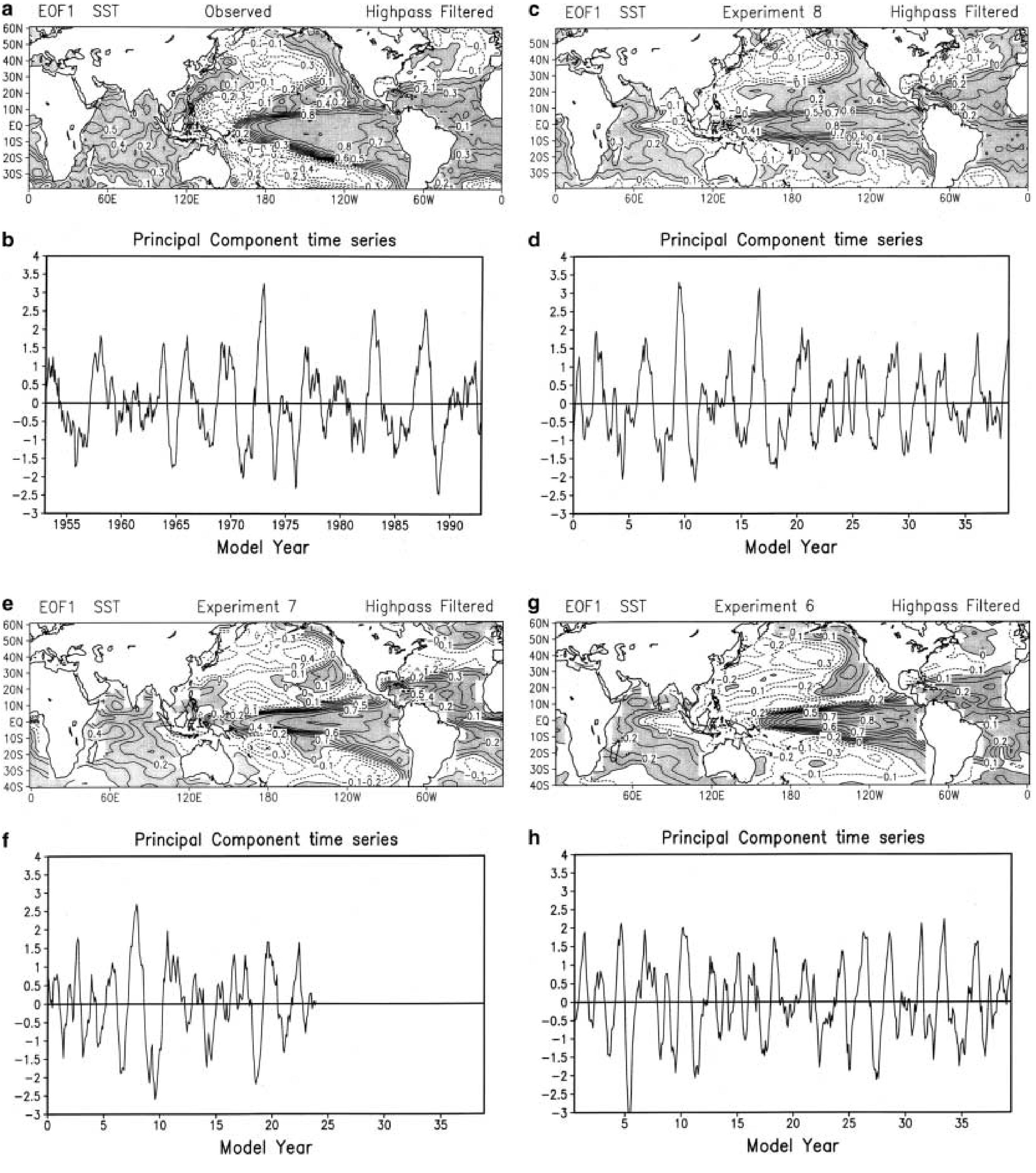

**Fig. 9** **a** EOF1 from highpass filtered monthly SST and **b** normalized principal component time series corresponding to EOF1, for the observations (1950–1995, Reynolds and Smith 1994). **c, d** Same as **a, b** except from experiment 8 (45 years). **e, f** Same as **a, b** except from experiment 7 (30 years). **g, h** Same as **a, b** except for experiment 6 (45 years). Note that 36 months from each end of the time series were cut off prior to the EOF analysis due to filtering

experiments (6, 7, and 8) and are shown in Fig. 10. Observations and model time series are 45 years except for CSM × 2′ which is 30 years. The observations use the interval 1950–94. Only the spectra for periods greater than one year are shown, though the first order autoregression red noise estimate and the 5% and 95% significance levels are calculated based on the entire monthly time series. The observations and the three

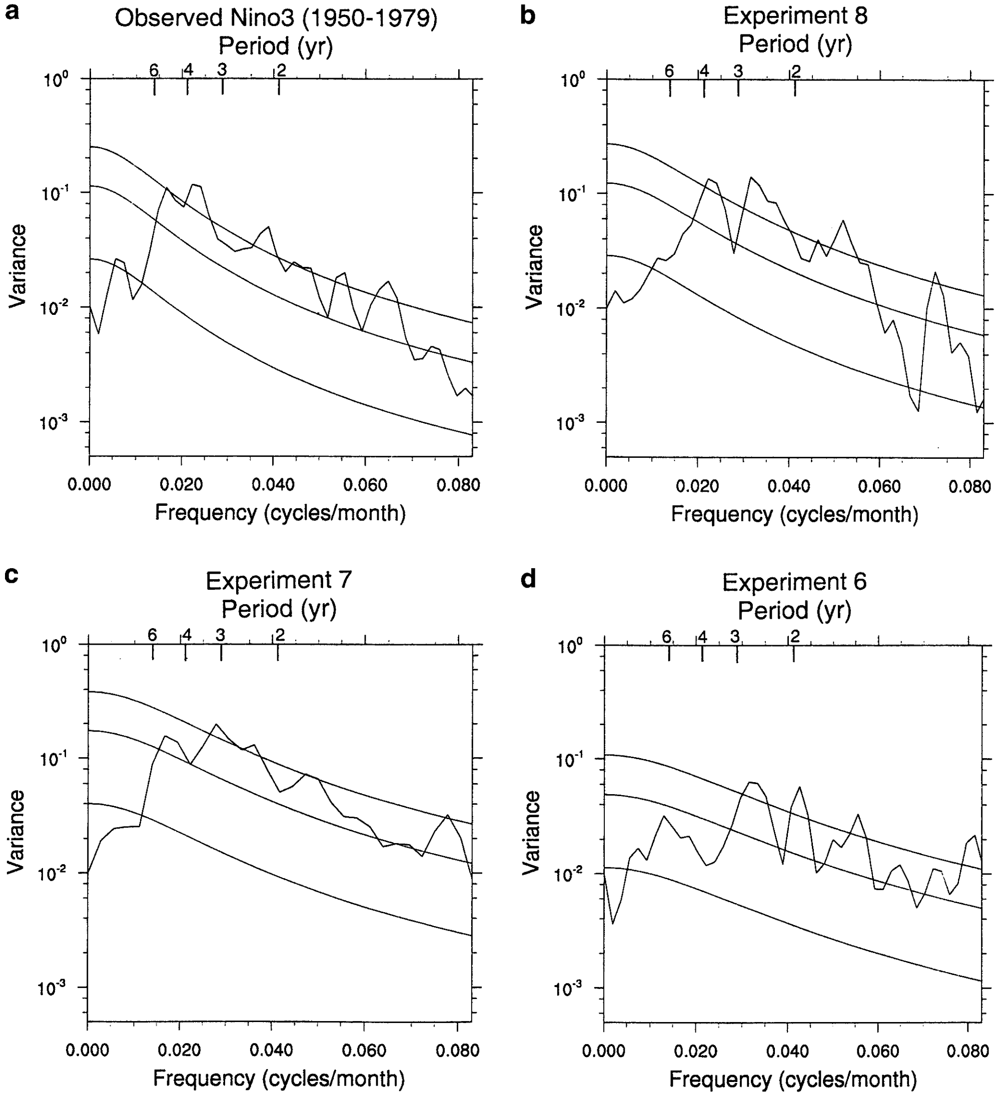

**Fig. 10** Spectra ($^{\circ}C^2 \times$ month) of monthly anomaly Nino3 SST time series from three representative model experiments for time series as noted in Fig. 9, and 1950–1994 for the observations. Only periods greater than one year are shown. The *thin smooth middle solid line* is the first order auto-regression estimate of red noise, *upper smooth line* is the 95% significance level, *lower smooth line* is 5% level, all calculated from the original monthly anomaly time series and shown here only for periods greater than one year

model experiments all show significant power at the typical El Nino periods around 3–6 years, and in the tropospheric biennial oscillation (TBO) period of somewhat greater than two years (e.g., Meehl 1997b; Meehl and Arblaster 1998). There is decadal variability in the exact manifestations of the spectral peaks in the El Nino frequencies in observations (e.g., Webster et al. 1998) and in the models analyzed for longer periods (e.g., Washington et al. 2000). The observations for this particular time period show power near the 3–6 year ENSO and 2.3 year TBO periods significant at greater than the 95% level. For experiment 8, there is enhanced power in the El Nino periods near four years and the TBO period of about 2.5 to 2.8 years. For experiment 7, there is significant power in the 3 to 4 year ENSO range, and at about 2.5 years for the TBO, and for experiment 6 around three years and two years, respectively. In fact, all ten experiments simulate significant El Nino-like variability in the range of the observed El Nino periods of roughly 3–5 years and in the TBO periods around 2–2.5 years as observed. However, the models tend toward the shorter ENSO periods of around 3–4 years as seen in some other global coupled models (e.g., Timmermann et al. 1999).

The Nino3 time series are representative of the larger scale patterns in Fig. 9. Correlations of the non-filtered monthly PC time series (nearly the same as the filtered patterns in Fig. 9 due to the dominance of ENSO) with the non-filtered monthly Nino3 SST time series are +0.80 for observations, +0.82 for experiment 6, +0.80 for experiment 7, and +0.89 for experiment 8, all significant at the 1% level.

## 5 Discussion and conclusions

A number of versions of two global coupled models, using the same atmospheric component but different ocean components, exhibit different amplitudes of El Nino-like variability in the equatorial Pacific, most directly influenced by the values of ocean background vertical diffusivity. The models with smaller background vertical diffusivity have larger El Nino amplitude. This is directly related to the simulation of the mean thermal structure of the equatorial upper ocean. All models have thermoclines that slope upward to the east as observed, but the models with larger amplitude El Nino-like variability have a more intense thermocline. Some models have a systematic error of a thermocline that is too shallow, but those models can still produce high El Nino variability. Taken together, these results imply that for a given wind variation, it is easier for equatorial upwelling to tap the colder sub-thermocline water and produce greater SST variability. The magnitude of the equatorial zonal wind stress also is associated with Nino3 SST amplitude. When wind stress is stronger, the east–west slope of the thermocline is greater, which can be associated with stronger equatorial east–west SST gradient. The enhanced thermocline slope brings it closer to the surface in the east, which increases the Nino3 SST interannual variability.

All versions have similar systematic errors in simulating the seasonal cycle in the eastern Pacific, with the equatorial SST evolution having a more semiannual character than the dominant annual period seen in observations, and a double ITCZ for much of the year in the eastern Pacific. Therefore, since all models have similar systematic errors in the simulation of the seasonal cycle, that does not seem to affect, or be affected by, the amplitude of El Nino in the models.

An EOF analysis of SSTs (filtered to retain variability at El Nino periods shorter than 8 years) for three representative experiments with $0.1\ \mathrm{cm}^2\ \mathrm{s}^{-1}$ background vertical diffusivity shows a systematic error of the eastern Pacific cold tongue regime extending too far into the western Pacific warm pool in the two experiments with relatively strong equatorial Pacific zonal wind stress. In contrast, the experiment representing those experiments with weaker wind stress has comparatively lower amplitude Nino3 variability but a somewhat better spatial simulation of the eastern Pacific cold tongue pattern. Spectra of the unfiltered monthly Nino3 anomalies for the models show power that falls within the observed range of ENSO periods of roughly 3–6 years and the TBO of about 2–2.5 years for the years 1950–94. However, the models tend to prefer ENSO periods of about 3–4 years at the lower end of the observed range. The Nino3 time series are significantly correlated to the respective PC time series of the first EOF of near-global SSTs, indicative of the close relationship between SST interannual variability in the eastern equatorial Pacific and the near-global patterns of SST in the models and observations.

**Acknowledgements** We thank William Large, Mojib Latif, Steve Wilson and an anonymous reviewer for their helpful comments. A portion of this study was supported by the Office of Biological and Environmental Research, US Department of Energy, as part of its Climate Change Prediction Program. The National Center for Atmospheric Research is sponsored by the National Science Foundation.

## References

Bonan GB (1998) The land surface climatology of the NCAR land surface model (LSM 1.0) coupled to the NCAR community climate model (CCM3). J Clim 11: 1307–1326

Boville B, Gent P (1998) The NCAR climate system model, Version 1. J Clim 11: 1115–1130

Gent P, Bryan F, Danabasoglu G, Doney S, Holland W, Large W, McWilliams J (1998) The NCAR climate system model global ocean component. J Clim 11: 1287–1306

Jones PD (1994) Hemispheric surface air temperature variations: a reanalysis and an update to 1993. J Clim 7: 1794–1802

Kiehl JT, Hack JJ, Bonan G, Boville B, Williamson D, Rasch P (1998) The National Center for Atmospheric Research community climate model (CCM3). J Clim 11: 1131–1149

Knutson TR, Manabe S (1998) Model assessment of decadal variability and trends in the tropical Pacific ocean. J Clim 11: 2273–2296

Large WG, Gent PR (1999) Validation of vertical mixing in an equatorial ocean model using large eddy simulations and observations. J Phys Oceanogr 29: 449–464

Large WG, Danabasoglu G, McWilliams JC, Gent PR, Bryan FO (2000) Equatorial circulation of a global ocean climate model with anisotropic horizontal viscosity. J Phys Oceanogr (in press)

Latif M, Sterl A, Maier-Reimer E, Junge WM (1993) Climate variability in a coupled GCM. Part I: the tropical Pacific. J Clim 6: 5–21

Lau N-C, Philander SGH, Nath MJ (1992) Simulation of ENSO-like phenomena with a low-resolution coupled GCM of the global ocean and atmosphere. J Clim 5: 284–307

Levitus S (1982) Climatological atlas of the world ocean. NOAA Prof Pap 13, National Oceanic and Atmospheric Administration, 173 pp

Li T (1997) On the phase transition of the El Nino-southern oscillation: a stationary SST mode. J Atmos Sci 54: 2872–2887

Ma C-C, Mechoso CR, Robertson AW, Arakawa A (1996) Peruvian stratus clouds and the tropical Pacific circulation: a coupled ocean-atmosphere GCM study. J Clim 9: 1635–1645

McPhaden M (1999) Genesis and evolution of the 1997–98 El Nino. Science 283: 950–954

Mechoso CR and 19 coauthors (1995) The seasonal cycle over the tropical Pacific in general circulation models. Mon Weather Rev 123: 2825–2838

Meehl GA (1990) Seasonal cycle forcing of El Nino-southern oscillation in a global coupled ocean-atmosphere GCM. J Clim 3: 72–98

Meehl GA (1997a) Modification of surface fluxes from component models in global coupled models. J Clim 10: 2811–2825

Meehl GA (1997b) The south Asian monsoon and the tropospheric biennial oscillation. J Clim 10: 1921–1943

Meehl GA, Arblaster JM (1998) The Asian–Australian monsoon and El Nino-southern oscillation in the NCAR climate system model. J Clim 11: 1357–1387

Meehl GA, Branstator GW, Washington WM (1993) Tropical Pacific interannual variability and $CO_2$ climate change. J Clim 6: 42–63

Nagai T, Tokioka T, Endoh M, Kitamura Y (1992) El Nino-southern oscillation simulated in an MRI atmosphere-ocean coupled general circulation model. J Clim 5: 1202–1233

Neelin JD (1991) The slow sea surface temperature mode and the fast-wave limit: analytic theory for tropical interannual oscillation and experiments in a hybrid coupled model. J Atmos Sci 48: 584–606

Neelin JD and coauthors (1992) Tropical air-sea interactions in general circulation models. Clim Dyn 7: 73–104

Otto-Bliesner BL (1999) El Nino/La Nina and Sahel precipitation during the middle Holocene. Geophys Res Lett 26: 87–90

Pontaud M, Ceron J-P, Pluviaud F (1998) Le sous-projet DIVCOP de CMIP: Compilation des resultats. Note de L'Enm, Unite Formation et Recherche 1, Ecole Nationale de la Meteorologie, Meteo France, 42 Ave. G. Coriolis, Toulouse-cedex, France

Reynolds RW, Smith TM (1994) Improved global sea temperature analyses using optimum interpolation. J Clim 7: 929–948

Roeckner E, Oberhuber JM, Bacher A, Christoph M, Kirchner I (1996) ENSO variability and atmospheric response in a global coupled atmosphere-ocean GCM. Clim Dyn 12: 737–754

Semtner AJ (2000) Ocean and climate modeling on advanced parallel computers: progress and prospects. Commun ACM (in press)

Sperber KR, Hameed S, Gates WL, Potter GL (1987) Southern oscillation simulated in a global climate model. Nature 329: 140–142

Tett S (1995) Simulation of El Niño/Southern oscillation-like variability in a global AOGCM and its response to $CO_2$ increase. J Clim 8: 1473–1502

Timmermann A, Oberhuber J, Bacher A, Esch M, Latif M, Roeckner E (1999) Increased El Nino frequency in a climate model forced by future greenhouse warming. Nature 398: 694–697

Trenberth KE (1997) The definition of El Nino. Bull Am Meteorol Soc 78: 2771–2777

Trenberth KE, Olson JG, Large WG (1989) A global ocean wind stress climatology based on ECMWF analyses. NCAR/TN-338 + STR, 93 pp

Wang B, Feng Z (1996) Chaotic oscillations of tropical climate: a dynamic system theory for ENSO. J Atmos Sci 51: 2786–2802

Washington WM, Weatherly JW, Meehl GA, Semtner Jr AJ, Bettge TW, Craig AP, Strand Jr WG, Arblaster JM, Wayland VB, James R, Zhang Y (2000) Parallel climate model (PCM) control and transient simulations. Clim Dyn (in press)

Weatherly JW, Briegleb BP, Large WG, Maslanik JA (1998) Sea ice and polar climate in the NCAR CSM. J Clim 11: 1472–1486

Webster PJ, Magana VO, Palmer TN, Shukla J, Tomas RA, Yanai M, Yasunari T (1998) Monsoon: processes, predictability, and the prospects for prediction. J Geophys Res 103: 14 451–14 510

Wilson SG (2000) How ocean vertical mixing and accumulation of warm surface water influence the "sharpness" of the equatorial thermocline. J Clim 13: 3638–3656

Xie P, Arkin PA (1996) Analyses of global monthly precipitation using gauge observations, satellite estimates, and numerical model predictions. J Clim 9: 840–858

Yu J-Y, Mechoso CR (1999) Links between annual variations of Peruvian stratocumulus clouds and of SST in the eastern equatorial Pacific. J Clim 12: 3305–3318

Yukimoto S, Endoh M, Kitamura Y, Kitoh A, Motoi T, Noda A, Tokioka T (1996) Interannual and interdecadal variabilities in the Pacific in an MRI coupled GCM. Clim Dyn 12: 667–683

Zebiak SE, Cane MA (1987) A model ENSO. Mon Weather Rev 115: 2262–2278